GeoScienceWorld
Lithosphere
Volume 2022, Article ID 3810988, 17 pages
https://doi.org/10.2113/2022/3810988

Lithosphere

Research Article

Research on Theory and Technology of Floor Heave Control in Semicoal Rock Roadway: Taking Longhu Coal Mine in Qitaihe Mining Area as an Example

Xuming Zhou,[1,2] Sheng Wang,[2] Xuelong Li,[1,2] Jingjing Meng,[3] Zhen Li,[2] Linhan Zhang,[2] Dongdong Pu,[4] and Longkang Wang[5]

[1]*Mine Disaster Prevention and Control-Ministry of State Key Laboratory Breeding Base, Shandong University of Science and Technology, Qingdao 266590, China*
[2]*College of Energy and Mining Engineering, Shandong University of Science and Technology, Qingdao 266590, China*
[3]*Department of Civil, Environmental and Natural Resources Engineering, Luleå University of Technology, Luleå, Sweden*
[4]*Zhengmei Group Engineering Technology Research Institute, Zhengzhou 450000, China*
[5]*China Center for Information Industry Development, Beijing 100048, China*

Correspondence should be addressed to Sheng Wang; 202082010032@sdust.edu.cn, Xuelong Li; lixlcumt@126.com, and Longkang Wang; 202120021046@cqu.edu.cn

Received 15 June 2022; Accepted 9 July 2022; Published 25 July 2022

Academic Editor: Shaofeng Wang

Copyright © 2022 Xuming Zhou et al. Exclusive Licensee GeoScienceWorld. Distributed under a Creative Commons Attribution License (CC BY 4.0).

As one of the most common disasters in deep mine roadway, floor heave has caused serious obstacles to mine transportation and normal production activities. The third section winch roadway in the third mining area of Qitaihe Longhu coal mine has a serious floor heave due to the large buried depths of the roadway and the semicoal rock roadway, and the maximum floor heave is 750 mm. For the problem of floor stability, this paper establishes a mechanical model to analyze the stability of roadway floor heave by analogy with the basement heave of deep foundation pit. It provides a model reference for analyzing the problem of roadway floor heave. Aiming at the problem of roadway floor heave in Longhu coal mine, the roadway model is established by using FLAC3D, and the roadway model after support is established according to the on-site support measures. Through the analysis of the distribution of roadway plastic area, stress nephogram, and displacement field simulation results, the results show that the maximum displacement of roadway roof and floor after support is reduced by 15% and 23%, but the maximum floor heave is still 770 mm, which is close to the measured floor heave of roadway. In order to solve the problem of roadway floor heave and integrate economic factors, this paper puts forward three support optimization schemes, simulates the support effect of each scheme, and finally determines that scheme 3 is the best support optimization scheme. Compared with that under the original support, the amount of floor heave is reduced by 81%, and the final amount of floor heave is 150 mm, which can meet the requirements of roadway floor deformation. The results provide a scheme and guidance for roadway support optimization.

1. Introduction

Floor heave is one of the most common phenomena in coal mine roadway, especially deep roadway. It is also an urgent engineering problem faced by underground mining, especially deep mining [1]. The bulging of the bottom plate usually causes serious deformation of the track, which poses a serious threat to the safe operation of the tramcar [2–4]. Due to the large buried depth of the roadway and most of it is coal seam roadway, this roadway is located in the protective coal pillar of the mountain, which has been in the stress concentration area of the mining area for a long time and is affected by mining [5, 6]. The floor heave of this roadway is very serious, the maximum floor heave is 900 mm,

Downloaded from http://pubs.geoscienceworld.org/gsa/lithosphere/article-pdf/doi/10.2113/2022/3810988/5659685/3810988.pdf
by guest

and the roadway must be unobstructed through roadway repair [7], which seriously restricts the efficient production of the coal mine.

Many scholars have conducted relevant research on the mechanism of roadway floor heave. Chang et al. [8] simulated the process of roadway floor heave by using similar material simulation test and put forward the support method of strengthening the bottom plate first, then supporting both sides and roof, and then strengthening the support of key parts (top and straight wall corner). Gao et al. [9] used SRM-UDEC Trigon joint numerical method to study the failure mechanism of roadway along unstable goaf, proved the asymmetry of roadway failure, and defined the main role of shear failure in roadway failure. Gao et al. [10] carried out numerical simulation, indoor physical simulation, and engineering practice; revealed the mechanism of roadway reinforcement roof and side wall to control roadway floor heave; and successfully controlled floor heave. Kang et al. [11] have shown that the floor angle pile + floor grouting support scheme can significantly improve the mechanical properties of floor rock mass and effectively control the deformation of roadway floor and two sides. Mo et al. [12] evaluated the potential of major floor heave for new mining projects or future roadway development by quantifying the stability of floor rock stratum by considering two main factors: uniaxial compressive strength of floor unit and structural plane spacing. Sun et al. [13] use infrared thermal imager and camera to capture the thermal response and displacement of roadway section and use circular strain gauge arranged in surrounding rock to measure the deformation of roadway section. The results show that horizontal stress has a great impact on floor heave failure, and rock mass failure is accompanied by abnormal temperature change. According to the long-term field monitoring, Liu et al. [14] proposed that the main reason for the floor heave of deep soft rock roadway is that the roadway floor in the open state has become the main place for roadway deformation and stress release, and the weak and broken rock strata in the floor squeeze into the roadway under the action of in situ stress to form a continuous plastic flow. Bai and Hou [15, 16] studied the movement characteristics of roadway floor strata at different depths through the combination of on-site borehole peeping, theoretical analysis, and numerical simulation and revealed the floor heave mechanism of shallow heave and deep subsidence. Li et al. [17, 18] studied the influence of the mechanical strength of the roadway roof rock on the roadway floor heave. Through numerical simulation, it can be seen that the mechanical strength of the roadway roof rock has an important influence on the roadway floor heave degree, the range of roadway plastic zone, and the stress distribution state of roadway surrounding rock. Therefore, it is proposed that strengthening the roof rock stratum can effectively control the floor heave of the roadway. The existing research on roadway floor heave pays more attention to the influencing factors of roadway floor heave and lacks the systematic sorting and derivation of roadway floor heave model.

In order to ensure the safe and efficient production of the mine and eliminate the interference of floor heave to the production as much as possible, predecessors put forward some methods to limit the occurrence and amount of floor heave on the basis of a lot of research and practice [19]. These methods are divided into support reinforcement method, pressure relief method, and combined support method according to their different mechanisms [20].

(1) The support and reinforcement method is to improve the strength of the surrounding rock of the bottom plate to resist the deformation of the bottom drum. This method is the most commonly used method to control the amount of kick. This method mainly includes adopting fully enclosed roadway support [21], concrete reverse arch [22], floor truss, adding floor anchor [23], and floor grouting [24]. This kind of method is generally applicable to the development of roadway, which is characterized by high support strength and average force on the surrounding rock of roadway floor

(2) The pressure relief method [25] can also effectively control the roadway floor heave, and its mechanism is different from the reinforcement method. Reinforcement method is to resist the stress of roadway surrounding rock and its support system by strengthening the strength of surrounding rock, which inevitably reduces the deformation of roadway floor surrounding rock. The roadway floor pressure relief law is to change the stress state of the roadway floor surrounding rock, so that the roadway floor surrounding rock is in the stress reduction area. If the stress is small, it will inevitably reduce the deformation of the roadway floor surrounding rock. The mechanism of controlling floor heave by pressure relief method is to transfer high stress to deep surrounding rock, so that the surrounding rock of roadway is in the stress reduction area [26]

(3) The combined support method [27, 28] is often used in combination with the above methods of controlling the in situ bottom drum. Moreover, each combination has its own scope of application. For example, when the surrounding rock of the floor is relatively weak and the in situ stress is large, the combined support method of blasting + closed support can be used. In high stress roadway, such as deep roadway and roadway strongly affected by mining, the combined support method of slit + bottom plate bolt is usually used, but in roadway with floor heave only because the floor rock is relatively weak; then, the combined support method of floor blasting and grouting can be used [29]

At present, treatment measures of roadway floor heave pay more attention to method innovation. Many scholars have also used various software to simulate the support effect. However, research into roadway floor heave mechanism model is relatively rare, and research into roadway floor heave of semicoal rock roadway is relatively less. In this paper, the floor heave of the three-stage winch roadway in

Downloaded from http://pubs.geoscienceworld.org/gsa/lithosphere/article-pdf/doi/10.2113/2022/3810988/5659685/3810988.pdf
by guest

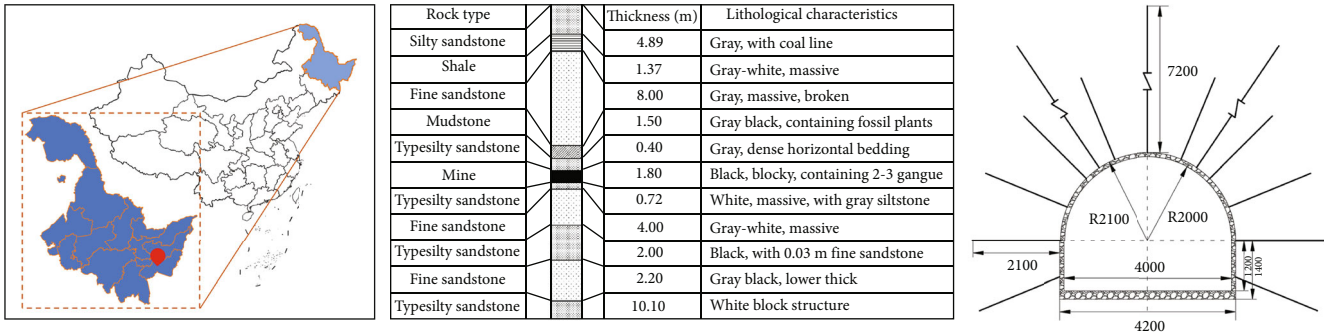

(a) Mine location (b) Rock stratum histogram of the third mining area (c) Roadway support form

Figure 1: Project background.

the third mining area of Longhu coal mine in Qitaihe was taken as the research object, and a mechanical model of the floor heave of the roadway was established based on the research results of the large foundation pit bottom protrusion. The model was improved according to the mechanical characteristics of the deep roadway, and the mechanism of the floor heave of the roadway was explained. Meantime, the floor heave problem of semicoal rock roadway in winch road was simulated, and the simulation results were compared with the field monitoring data to determine the simulation effect. On this basis, the improvement measures of roadway support were put forward, and the effect of support improvement measures was simulated through numerical simulation. The results provide a scheme for the next support optimization work of the mine.

2. Project Overview and Requirements

Qitaihe Longhu coal mine is located at the east end of Qitaihe coalfield in Heilongjiang Province, as shown in Figure 1(a). The mining depth of the third mining area of the mine is 731~785 m, the strike of coal (rock) layer is 275°, the dip is 185°, the dip angle is 3° ~35°, and the average coal thickness is 1.8 m. The specific distribution of rock stratum is shown in Figure 1(b). The downhill slope of the track in this area is -21°, which is excavated along the coal seam floor and belongs to semicoal rock roadway [30]. The section is a straight wall semicircular arch, the roadway is 4.2 m wide, the straight wall is 1.2 m high, and the net area of the roadway is 11.08 m^2. The support form of this roadway is bolt shotcrete, and the bolt is adopted Φ22 left hand screw thread steel anchor bolt, with length of 2.2 m, anchor depth of 2.1 m, and anchor length of 0.7 m, and adopts end anchor with anchor force of 60 kN and row spacing and spacing of 800 mm. The type of anchor cable is 1680 low relaxation steel strand, with a length of 7.2 m and an anchor length of 1.2 m. It is arranged in a diamond shape, with a longitudinal length of 1.6 m and a transverse length of 2.4 m. The section form and support parameters are shown in Figure 1(c).

As the roadway is downhill by rail, it serves the whole mining area and has a long service life. However, this roadway is also a semicoal rock roadway. On the one hand, the mechanical strength of its roof and floor, especially the rock mass of the two sides, is lower than that of the surrounding rock of the general whole rock roadway, and it is easier to be damaged under the action of surrounding rock stress. On the other hand, part of the upper working face of the mining area has been mined, so that the upper part of the roadway is in the uphill protective coal pillar for a long time, so that the stress concentration factor of the surrounding rock of the roadway is large [31]. The surrounding rock of this roadway is subjected to high surrounding rock stress for a long time and mining pressure in the mining area at the same time. The surrounding rock deformation is serious, the bolt fails in a large area, and the concrete spray layer falls off in a large area, in which the floor heave is very serious. The maximum floor heave in the middle and upper part of the roadway is 900 mm, and the track laid in the roadway is seriously deformed, which seriously affects the normal use of the roadway. In order to ensure the normal production of several working faces in the deeper part of the mining area, it has to organize multiple bottom pulling, which wastes a lot of manpower and material resources. At the same time, it is necessary to optimize the support scheme on the basis of the original support to control the floor heave of the roadway and ensure the normal production of the mine.

3. Basic Mechanical Parameters of Confining Pressure

3.1. Determination of Physical and Mechanical Parameters of Rock Samples. The mechanical properties of roadway surrounding rock largely determine the stability classification of roadway surrounding rock. At the same time, the mechanical parameters of surrounding rock are also the basic parameters for the selection of mining engineering equipment, the selection of blasting parameters, numerical simulation calculation, and the optimization of reasonable support mode of roadway. Therefore, in order to carry out various work in the future, the physical and mechanical parameters of roadway surrounding rock must be measured. Therefore, in the section with serious floor heave on site, the top and bottom plates and two sides are sampled, and the obtained rock samples are sealed with plastic film. The coal and rock samples obtained are shown in Table 1.

Using the rock mechanics test system of the rock mechanics laboratory of the school of resources and environmental engineering of Heilongjiang University of science

Downloaded from http://pubs.geoscienceworld.org/gsa/lithosphere/article-pdf/doi/10.2113/2022/3810988/5659685/3810988.pdf
by guest

Table 1: Site sampling records.

Sample code	Coal rock type	Horizon	Rock sample characteristics
A	Fine sandstone	Main roof	Gray, block crushing, with 0.5 ~ 1.5 mm cracks
B	Siltstone	Immediate roof	Dark gray
C	Mudstone	Two sides	Gray, dense, horizontal bedding
D	73# coal	Two sides	Black, blocky
E	Siltstone	Immediate bottom	White block with argillaceous
F	Fine sandstone	Main bottom	Grayish white, bedding, joint

Figure 2: Rock mechanic test system.

and Technology (Figure 2), and in accordance with the provisions of the Chinese coal industry standard MT38-48-87 "Determination method of physical and mechanical properties of coal and rock," the rock samples obtained from the three section winch in the third mining area are processed, and their physical and mechanical parameters are measured [32–34].

In the experiment, the firmness coefficient of the rock sample is measured by the tamping method. The tensile strength and compressive strength of the rock sample are measured by the splitting method and uniaxial compression test, respectively. The cohesion and internal friction angles of the rock sample are measured by the ordinary compression test. The deformation modulus and elastic modulus of the rock sample are calculated through the stress-strain curve of the uniaxial compression test, and the results in Table 2 are obtained [35].

3.2. Determination of Physical and Mechanical Parameters of Rock Mass. Because rock mass is composed of rock block and structural plane, and the strength of structural plane is much smaller than that of rock block, the strength of rock mass is much smaller than that of rock block. However, due to the limitation of underground field test and the variability of occurrence environment, it is too complex to obtain the real rock mass strength parameters, so the rock mass strength is generally estimated with the help of laboratory experiments and statistics. However, if the numerical value of coal and rock blocks obtained from laboratory test is brought into the numerical simulation, the results will be very different from the actual results. Therefore, in order to improve the accuracy of numerical simulation, the mechanical parameters of coal and rock blocks must be reduced [36, 37]. Bulk modulus K and shear modulus G are also used in numerical simulation. K and G can be determined by elastic modulus E and Poisson's ratio μ according to the following equations.

$$K = \frac{E}{3(1-2\mu)}, \tag{1}$$

$$G = \frac{E}{2(1-\mu)}. \tag{2}$$

Finally, Table 3 is obtained as the data to be used in the numerical simulation in the next chapter. It is difficult to test the elastic modulus and internal friction angle of coal [38].

3.3. Determination of Vertical Original Rock Stress. The buried depth of the third section of the winch Lane in the third mining area is between 731 and 785 m, but the roadway is within the protective coal pillar up the mountain. In the stress concentration area of this mining area, the width of protective coal pillar is less than 50 m, and the surrounding rock of roadway is greatly affected by mining. Therefore, it is not enough to simply consider the buried depth of the roadway when calculating the vertical surrounding rock stress of the roadway. In order to accurately calculate the vertical surrounding rock stress of the roadway as much as possible, the influence of the mining influence coefficient must be considered, and the mining influence coefficient K is taken as 1.43; then, the theoretical equivalent buried depth of the three sections of the winch in the third mining area: $H = 1045\,\text{m} \sim 1122\,\text{m}$ [39, 40]. According to the relationship between vertical stress and vertical depth (equation (3)), it can be seen that the vertical stress borne by the surrounding rock of this roadway is very large.

$$\sigma_z = \gamma H, \tag{3}$$

where H is the corresponding value in the corresponding section, and γ is equal to l 27 kN/m^2.

Before excavation, the vertical original rock stress of the winch roadway in the third section of the third mining area is about 28.23 MPa~30.31 MPa.

4. Stability Analysis of Bottom Plate

4.1. Types of Roadway Floor Heave. Floor heave is a common phenomenon in current coal mine production, especially in deep mines. According to the squeezing amount of the roadway

Downloaded from http://pubs.geoscienceworld.org/gsa/lithosphere/article-pdf/doi/10.2113/2022/3810988/5659685/3810988.pdf
by guest

Table 2: Measurement results of physical and mechanical parameters of coal and rock.

Name	Main roof fine sandstone	Immediate roof siltstone	Mudstone	Coal	Immediate bottom siltstone	Main bottom fine sandstone
Tensile strength/MPa	2.4	2.0	1.8	1.42	2.0	2.4
Uniaxial compressive strength/MPa	78	69	45	2	58	72
Modulus of elasticity/GPa	10.34	10.1	9.7	2.41	10.1	10.3
Deformation modulus/GPa	8.4	8.0	6.3	1.61	8.0	8.2
Internal friction angle/(°)	48	40	30	29	35	42
Cohesion/MPa	16	14	8	4.42	13	14

Table 3: Physical and mechanical parameters of coal and rock after reduction.

Name	Main roof fine sandstone	Immediate roof siltstone	Mudstone	Coal	Immediate bottom siltstone	Main bottom fine sandstone
Tensile strength/MPa	1.1	1.0	0.9	0.5	1.0	1.1
Uniaxial compressive strength/MPa	21.84	19..6	12.6	2	16.24	20.45
Bulk modulus/MPa	8.86	2.0	3.6	0.5	7.75	8.84
Shear modulus/MPa	7.95	6.42	2.96	0.8	3.76	7.85
Internal friction angle/(°)	48	40	30	29	35	42
Cohesion/MPa	6.5	6.0	0.4	0.6	5.2	5.6

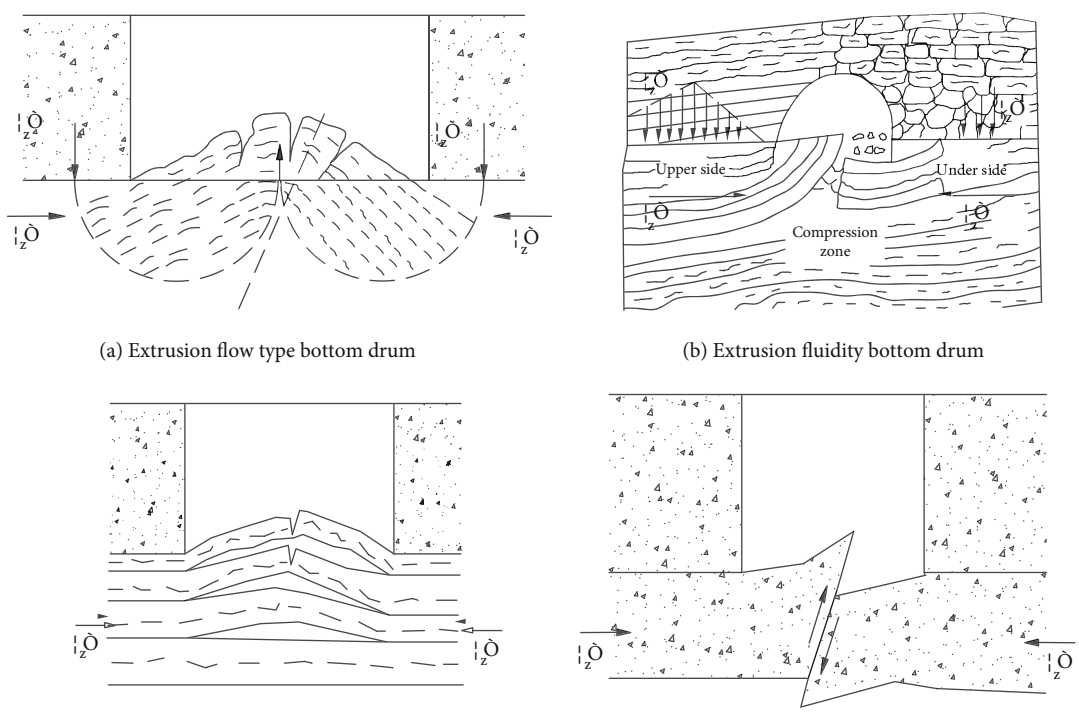

(a) Extrusion flow type bottom drum

(b) Extrusion fluidity bottom drum

(c) Flexure folding floor drum

(d) Shear dislocation floor drum

Figure 3: Type of roadway floor heave [38].

floor into the roadway space and the impact on the normal use of the roadway, the roadway floor heave can be divided into slight floor heave (100 mm~200 mm), obvious floor heave (200 mm~300 mm), serious floor heave (300 mm~500 mm), and destructive floor heave (500 mm~800 mm). If the latter three floor heaves are not repaired in time, they will affect the normal use of the roadway and even cause safety accidents [41]. Shown in Figure 3, according to the failure mode

Downloaded from http://pubs.geoscienceworld.org/gsa/lithosphere/article-pdf/doi/10.2113/2022/3810988/5659685/3810988.pdf
by guest

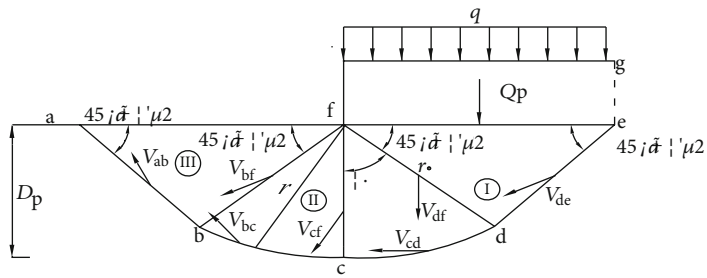

Figure 4: Failure mode diagram of roadway floor rock mass.

and formation mechanism, the bottom drum can be divided into the following types [42, 43]: the extrusion fluidity bottom drum, the flexure folding floor drum, the shear dislocation floor drum, and the water swelling floor drum.

4.2. Mechanical Model of Roadway Floor Heave. The phenomenon of roadway floor heave is similar to that of deep foundation pit base heave in geotechnical engineering [44, 45], and the research on the phenomenon of deep foundation pit base heave is more thorough and the theory is more mature. Therefore, based on the existing theoretical results of foundation heave of deep foundation pit, and combined with the difference between soil and rock, the model is modified.

The fundamental mechanism of the heave of the roadway floor is that the superposition of the stress transmitted from the two sides of the roadway rock mass to the floor rock mass and the stress transmitted by the deep rock mass of the floor exceeds the stress that the roadway floor rock mass can bear, the floor rock mass will break and form a sliding crack surface, and the floor rock mass will squeeze into the roadway space along this sliding crack under the action of stress, resulting in the generation of floor heave [46]. From the fundamental mechanism of roadway floor heave, in order to solve whether the roadway floor heaves, we must start from the perspective of the ultimate bearing capacity of the rock mass of the roadway floor [47]. The stability analysis of roadway floor heave should essentially be the limit equilibrium problem of rock mass [48]. Therefore, based on the limit analysis theory of plastic mechanics, a more reasonable solution should be obtained. Therefore, this paper follows the fundamental mechanism of the extrusion flow type floor heave problem and is based on the upper bound analysis theory of plastic mechanics. First, the basic failure mode is established from the sliding surface of prandel Risner solution. Second, the Mohr Coulomb yield criterion is introduced to obtain the flow method, so as to obtain the coordinated velocity field in the plastic zone, and then, the ultimate bearing capacity of the roadway floor is obtained through the virtual power principle. Then divide the stress on the roadway floor by the ultimate bearing capacity of the roadway floor, that is, the safety factor of the uplift and stability of the roadway bottom can be obtained.

4.2.1. Failure Mode of Rock Mass in Roadway Floor. In order to better answer and ignore the influence of secondary factors, we can make the following assumptions: (a) the rock mass below the roadway floor can resist the uplift of the roadway floor. If the rock mass of the roadway floor is not enough to resist the uplift of the roadway floor, the rock mass of the floor will slide along the bottom of the floor. (b) The vertical load Q_S on the two sides of the roadway and the horizontal stress on the rock mass of the roadway floor exceed the limit load Q_P that the rock mass below the two sides of the roadway can bear, which are the main factors causing the uplift of the rock mass of the roadway floor. (c) It is assumed that the sliding of the roadway floor rock mass is along the sliding fracture surface of prandel Risner solution, and three sliding fracture rock masses of active zone I, transition zone II, and passive zone III shown in Figure 4 are formed. The size of each sliding fracture rock mass area is determined by the load on the roadway floor rock mass and the lithology of the floor rock mass. (d) It is assumed that the vertical load on both sides of the roadway is uniformly distributed load V_{df}. (e) The influence of groundwater on roadway floor heave is not considered [49].

Figure 4 shows the failure mode diagram of roadway floor rock mass, in which the bottom curve of area II is a logarithmic spiral curve, and the equation expression is $r = r_0 e^{\Psi \tan \Phi'}$; ab, bc, cd, de, bf, and df are the slip surfaces of passive zone, transition zone, and active zone, respectively.

4.2.2. Rock Mass Flow Rule under Mohr Coulomb Yield Criterion. According to Mohr Coulomb yield criterion [50], the expression of sliding surface of rock mass is as follows:

$$f(\tau, \sigma) = \tau - c' - \sigma \tan \phi' = 0, \tag{4}$$

where τ is the shear stress of the shear slip surface; σ is the normal stress of shear slip surface; c' is the effective cohesion of rock; Φ' is the effective internal friction angle of rock; c' and Φ' are in weighted average values, when setting the floor rock mass as ideal plastic.

Taking any side from ab, bc, cd, and de, we can obtain the plastic potential equation [51].

$$d\varepsilon_n^p = d\lambda \frac{\partial f}{\partial \sigma}\,;\, d\varepsilon_h^p = d\lambda \frac{\partial f}{\partial \tau}, \tag{5}$$

where ε_n^p and ε_h^p are the normal strain and tangential strain on each sliding surface, respectively; f-plastic potential

Downloaded from http://pubs.geoscienceworld.org/gsa/lithosphere/article-pdf/doi/10.2113/2022/3810988/5659685/3810988.pdf
by guest

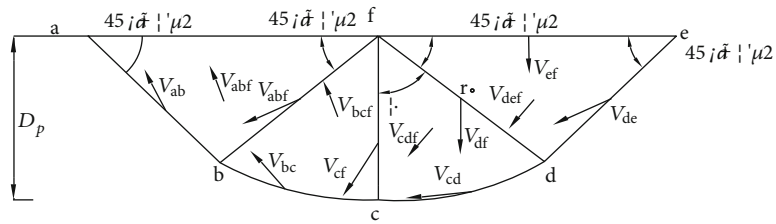

Figure 5: Schematic diagram of plastic velocity field.

function; $d\lambda$—constant is positive and non-negative scale factor.

Available $d\varepsilon_n^p/dt = \partial v_x/\partial x$, $d\varepsilon_h^p/dt = \partial v_y/\partial y$ from

$$\frac{d\varepsilon_n^p}{d\varepsilon_h^p} = \frac{\partial v_x/\partial x}{\partial v_y/\partial y} = -\tan\phi', \tag{6}$$

where normal and tangential directions of x, $y - ab$, bc, cd, de, cf, and df; v_x, v_y—normal deformation velocity and tangential deformation velocity of a point in ab, bc, cd, de, cf, and df; t —time.

Thus, the special solution of a set of velocity fields in (6) is

$$\left.\begin{aligned} v_x &= -E\tan\phi' x - E\tan\phi' y \\ v_y &= Ex + Ey \end{aligned}\right\}, \tag{7}$$

E is any constant that is not equal to zero. From equation (7), we can also get

$$\frac{v_x}{v_y} = -\tan\phi'. \tag{8}$$

In order to make equation (7), a practical solution that can be used, we must obtain the value of E. In order to obtain the value of E, we can add such a condition: the velocity field of each sliding surface is a coordinated velocity field. The solved velocity field can satisfy both the plastic flow law and the displacement coordination condition. Next, we will solve this coordinated velocity field:

$$\left.\begin{aligned} \overrightarrow{V_{ab}} &= \overrightarrow{V_{bf}} + \overrightarrow{V_{bc}} \\ \overrightarrow{V_{bc}} &= \overrightarrow{V_{cf}} + \overrightarrow{V_{cd}} \\ \overrightarrow{V_{cd}} &= \overrightarrow{V_{df}} + \overrightarrow{V_{de}} \end{aligned}\right\}. \tag{9}$$

4.2.3. Solution of Coordinated Velocity Field. In order to better rescue and coordinate the velocity field, the following provisions must be made: take the velocity field at the center of each slip surface as the representative value of the velocity field of each slip surface. Adding a cf plane in region II to participate in the calculation of coordinated velocity field is mainly because the bottom curve of region II is long, and increasing the cf plane is conducive to improving the accuracy.

The coordinated plastic velocity field can be realized by the principle of vector analysis, and its basic rules can be expressed by a set of vector equations (as shown in Figure 5).

According to equation (10) and Figure 5, a coordinated velocity field between each sliding surface can be obtained as follows:

$$\begin{gathered} V_{bf} = a_1 V_{ab},\ V_{bc} = a_2 V_{ab},\ V_{cf} = b_1 a_2 V_{ab}, \\ V_{cd} = b_2 a_2 V_{ab},\ V_{df} = c_1 b_2 a_2 V_{ab},\ V_{de} = c_2 b_2 a_2 V_{ab}, \\ a_1 = \frac{[\cos(\beta_{ab}) - \sin(\beta_{ab})\cot(\beta_{bc})]}{\left[\cos\left(\beta_{bf}\right) - \sin\left(\beta_{bf}\right)\cot(\beta_{bc})\right]}, \\ a_2 = \frac{\left[\sin(\beta_{ab}) - a_1\sin\left(\beta_{bf}\right)\right]}{\sin(\beta_{bc})}, \\ b_1 = \frac{[\cos(\beta_{bc}) - \sin(\beta_{bc})\cot(\beta_{cd})]}{\left[\cos\left(\beta_{cf}\right) - \sin\left(\beta_{cf}\right)\cot(\beta_{cd})\right]}, \\ b_2 = \frac{\left[\sin(\beta_{bc}) - b_1\sin\left(\beta_{cf}\right)\right]}{\sin(\beta_{cd})}, \\ c_1 = \frac{[\cos(\beta_{cd}) - \sin(\beta_{cd})\cot(\alpha_{de})]}{\left[\cos\left(\beta_{df}\right) - \sin\left(\beta_{df}\right)\cot(\beta_{de})\right]}, \\ c_2 = \frac{\left[\sin(\beta_{cd}) - c_1\sin\left(\beta_{df}\right)\right]}{\sin(\beta_{de})}. \end{gathered} \tag{10}$$

In equations (8) and (9): V_{ab}, V_{bc}, V_{cf}, V_{cd}, V_{df}, and V_{de} are the plastic velocity field at the center of the corresponding subscript slip surface; β_{ab}, β_{bf}, β_{bc}, β_{cf}, β_{cd}, β_{df}, and β_{de} are the dip angle of the plastic velocity field of the corresponding subscript slip surface.

It can be seen from the above that the center of gravity velocity fields of abf, bcf, cdf, and def are also solved with the above coordination conditions:

$$\left.\begin{aligned} \overrightarrow{V_{abf}} &= \overrightarrow{V_{ab}} + \overrightarrow{V_{bf}}, \overrightarrow{V_{bcf}} = \overrightarrow{V_{bf}} + \overrightarrow{V_{bc}} \\ \overrightarrow{V_{cdf}} &= \overrightarrow{V_{cf}} + \overrightarrow{V_{cd}}, \overrightarrow{V_{def}} = \overrightarrow{V_{df}} + \overrightarrow{V_{de}} \end{aligned}\right\}, \tag{11}$$

where $\overrightarrow{V_{abf}}$, $\overrightarrow{V_{bcf}}$, $\overrightarrow{V_{cdf}}$ and $\overrightarrow{V_{def}}$ are the center of gravity velocity vectors of abf, bcf, cdf, and def, respectively.

In addition, since we want to study the floor heave of the roadway, the vertical component of the gravity velocity field

Downloaded from http://pubs.geoscienceworld.org/gsa/lithosphere/article-pdf/doi/10.2113/2022/3810988/5659685/3810988.pdf
by guest

in each region is the solution we require. Therefore, as long as we consider the vertical component of the gravity velocity field in these four regions, we can get from equation (10) and equation (11):

$$\begin{aligned}
&\left(V_{abf}\right)^{v} = d_1 V_{ab}, \left(V_{bcf}\right)^{v} = d_2 V_{ab},\\
&\left(V_{cdf}\right)^{v} = d_3 V_{ab}, \left(V_{def}\right)^{v} = d_4 V_{ab},\\
&d_1 = -\left[\sin\left(\beta_{ab}\right) + a_1 \sin\left(\beta_{bf}\right)\right],\\
&d_2 = -\left[a_1 \sin\left(\beta_{bf}\right) + a_2 \sin\left(\beta_{bc}\right)\right],\\
&d_3 = -\left[b_1 a_2 \sin\left(\beta_{cf}\right) + b_2 a_2 \sin\left(\beta_{cd}\right)\right],\\
&d_4 = -\left[c_1 b_2 a_2 \sin\left(\beta_{af}\right) + c_2 b_2 a_2 \sin\left(\beta_{de}\right)\right],
\end{aligned} \tag{12}$$

where $(V_{abf})^{v}$, $(V_{bcf})^{v}$, $(V_{cdf})^{v}$, and $(V_{def})^{v}$ represent the vertical components of the gravity velocity field of abf, bcf, cdf, and def, respectively, which are positive downward and negative upward.

For the velocity field at the bottom of roadway slope V_{ef}, its direction is vertical downward, so it can only be solved approximately. Since the rock mass def mainly slides along the de plane, it means that V_{de} is the main control factor of the movement of def. Therefore, if we assume that the "V_{ef} equal V_{de} vertical component" should have an acceptable error, we can get

$$\left\{\begin{aligned} V_{ef} &= d_5 V_{ab}\\ d_5 &= -c_2 b_2 a_2 \sin\left(\beta_{de}\right)\end{aligned}\right\}. \tag{13}$$

4.2.4. Solution of Stability Coefficient of Bottom Drum. Solution of ultimate bearing capacity of roadway side base.

In the following, the virtual power principle is applied to solve the ultimate bearing capacity of roadway slope and bottom. First, the internal energy dissipation value of sliding fractured rock mass is calculated.

The unit of dissipated energy for any slip surface of rock mass is dM:

$$dM = \tau v_y + \sigma_x. \tag{14}$$

From equation (7), $v_x = -v \sin\phi'$, $v_y = -v \cos\phi'$ where v represents the plastic velocity, substitute the above equation into (14) and apply equation (1), including

$$dM = \left(\tau \cos\phi' - \sigma \sin\phi'\right) V. \tag{15}$$

We can know that when calculating the average velocity field of a sliding surface, we can approximately take the velocity field of the central point of the sliding surface as the average velocity field of each sliding surface. Therefore, v in (15) becomes a constant on the sliding surface. Then, the internal energy dissipation of the sliding surface can be obtained by multiplying the dissipated energy dM per unit area by the length of the sliding surface.

$$\left.\begin{aligned}
&\sum M = V_{ab} F\\
&F = \left|l_{ab} D\right| + \left|a_1 l_{bf} D\right| + \left|a_2 \widehat{l}_{bc} D\right| + \left|b_1 a_2 l_{cf} D\right| +\\
&\left|b_2 a_2 l_{cd} D\right| + \left|c_1 b_2 a_2 l_{df} D\right| + \left|c_2 b_2 a_2 l_{de} D\right|\\
&D = \tau \cos\phi' - \sigma \sin\phi'
\end{aligned}\right\}. \tag{16}$$

It can be known from plastic mechanics that in the maneuvering field, the generalized internal force always does positive work in its corresponding velocity field. Therefore, the internal energy dissipation value of each sliding surface in (16) takes the absolute value.

The work done by the external force includes the work done by the external load Q_p, the self weight of the sliding rock mass, and the vertical component of the horizontal tectonic stress on the sliding surface. From equation (12) and equation (13), the total work done by the external force is

$$\left.\begin{aligned}
&\sum \Pi = V_{ab}\begin{pmatrix} Q_P d_5 + \gamma S_{abf} d_1 + \gamma S_{bcf} d_2 + \gamma S_{cdf} d_3 + \gamma S_{def} d_4 +\\ \sigma_h \cos\alpha \sin\alpha d_1 + \sigma_h \cos\alpha \sin\alpha d_2 +\\ \sigma_h \cos\alpha \sin\alpha d_3 + \sigma_h \cos\alpha \sin\alpha d_4 \end{pmatrix}\\
&\alpha = 45^\circ - \frac{\phi'}{2}\\
&S_{abf} = l_{af} l_{ab} \sin\frac{\left(45^\circ - \phi'/2\right)}{2}\\
&S_{def} = l_{ef} l_{de} \sin\frac{\left(45^\circ + \left(\phi'/2\right)\right)}{2}\\
&S_{bcf} = D_p^2\left(\left(e^{\tan\phi'\left(45^\circ - \phi'/2\right)\pi/90^\circ} - 1\right)\left(4\tan\phi'\right)\right)\\
&S_{bcf} = \frac{\pi D_p^2}{8}\left(\phi' = 0\right)\\
&S_{bcf} = l_{df}^2\left(\frac{\left(e^{\tan\phi'\left(45^\circ - \phi'/2\right)\pi/90^\circ} - 1\right)}{\left(4\tan\phi'\right)}\right)\\
&S_{abf} = \frac{\pi l_{df}^2}{8}\left(\phi' = 0\right)
\end{aligned}\right\}, \tag{17}$$

In equation (17), S_{abf}, S_{bcf}, S_{cdf}, and S_{def}, respectively, represent the area of each area corresponding to the subscript; γ represents the weighted average value of the gravity in the sliding rock body, and σ_h is the horizontal stress.

According to the principle of virtual power, the total internal energy consumption dispersion $\sum M$ of sliding fractured rock mass should be equal to the work $\sum \prod$ done by all external forces on sliding fractured rock mass, so it can be obtained from equations (16) and (17)

Downloaded from http://pubs.geoscienceworld.org/gsa/lithosphere/article-pdf/doi/10.2113/2022/3810988/5659685/3810988.pdf
by guest

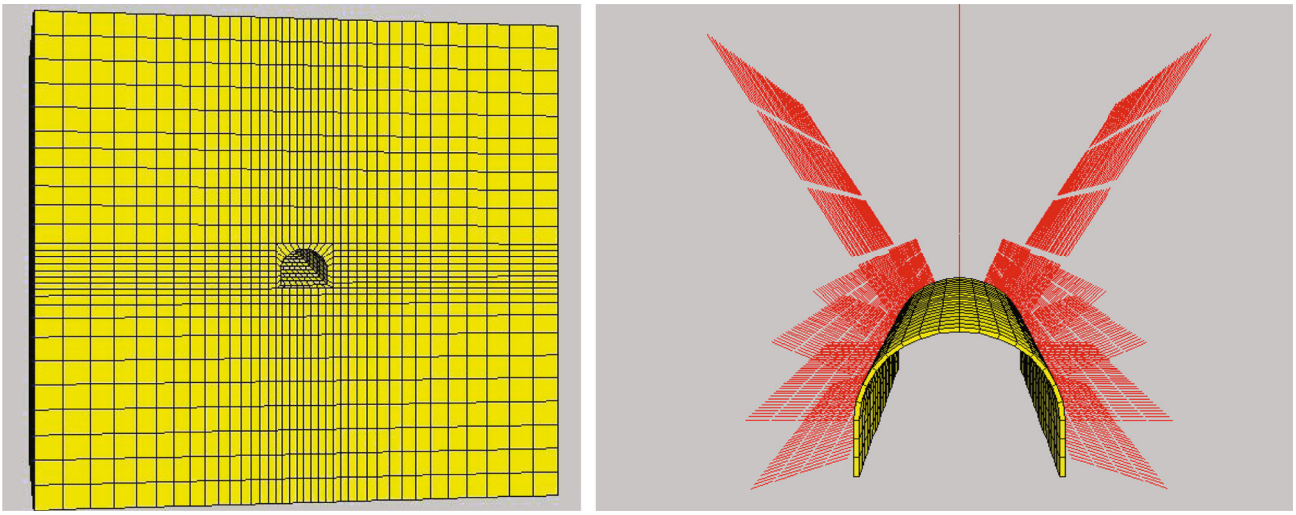

(a) Roadway model (b) Original roadway support drawing

Figure 6: Simulation model diagram.

$$F = \left(Q_P d_5 + \gamma S_{abf} d_1 + \gamma S_{bcf} d_2 + \gamma S_{cdf} d_3 + \gamma S_{def} d_4 + \sigma_h d_1 \cos\alpha \sin\alpha (d_1 + d_2 + d_3 + d_4) \right), \tag{18}$$

$$Q_P = \frac{\left(F - \left[\gamma S_{abf} d_1 + \gamma S_{bcf} d_2 + \gamma S_{cdf} d_3 + \gamma S_{def} d_4 + \sigma_h d_1 \cos\alpha \sin\alpha (d_1 + d_2 + d_3 + d_4) \right] \right)}{d_5}. \tag{19}$$

Equation (19) is the calculation equation of ultimate bearing capacity of roadway floor:

$$Q_s = q l_{ef}, \tag{20}$$

$$K = \frac{Q_P}{Q_S}. \tag{21}$$

Equation (21) is the safety factor of roadway floor heave. If it is less than 1, it means that the ultimate bearing capacity of roadway floor is lower than the applied value of load on the floor, and the roadway floor will heave.

5. Numerical Simulation Study

5.1. Model Establishment. The model shown in Figure 6 is established according to the actual site geology. The model is 50 m long, 29.4 m wide, and 42 m high. The roadway is at an angle of 21° with the horizontal direction. Because there are many strata and the mechanical parameters of each stratum are different, the model is established according to the layered combination of Figure 1(b) and Table 1. In order to reflect the actual situation as much as possible and reduce the number of units as much as possible, single precision division is adopted in grid division, so as to reduce the number of units, reduce running time. Finally, a total of 20240 units, 22470 nodes, and 2470 support structure units are formed. The model diagram is shown in Figure 5. The selection of rock mass parameters of each rock stratum in the model reflects the structural and strength characteristics of on-site rock mass. The selection of mechanical parameters is shown in Table 3.

The function and deficiency of the original support system are analyzed through the changes of stress and displacement of roadway surrounding rock under the action of no support and original support. Based on this, a new support method is put forward. The stress and strain of roadway surrounding rock under these new support schemes are simulated one by one, so as to select the optimal support scheme [52].

5.2. Simulation Results

5.2.1. Simulation Analysis of Original Support. To optimize the original roadway support parameters, we must master the failure process and stress distribution of surrounding rock under the original support parameters. Here, the Mohr model of FLAC3D is used to analyze the failure and stress distribution of roadway under the original support parameters.

Figure 7 shows the distribution of plastic zone of the roadway before and after the original support of the roadway. It can be seen from Figure 6(a) that the plastic zone of the unsupported roadway has developed greatly, and most units have been damaged by shear. Compared with the single surrounding rock roadway, the loose circle around the semicoal rock roadway shows obvious boundaries, and the

Downloaded from http://pubs.geoscienceworld.org/gsa/lithosphere/article-pdf/doi/10.2113/2022/3810988/5659685/3810988.pdf
by guest

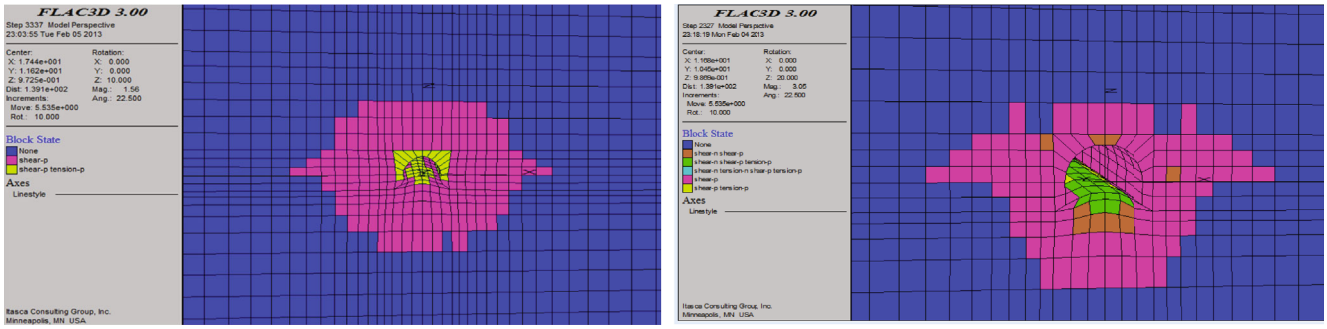

(a) Unsupported (b) Original support

Figure 7: Distribution of plastic zone.

loose circle in the upper part is significantly larger than that in the lower part. Moreover, it can be clearly seen from the figure that the roadway has been seriously deformed and the floor heave is very large. It can be seen from Figure 6(b) that under the action of the original support, the plastic area of the roadway is greatly reduced, mainly in the roof and two sides. However, the plastic area and floor plastic area of the two sides of mudstone are not significantly reduced, which is mainly due to the low strength of mudstone, which is easy to be damaged, and the mudstone is located in the bearing zone between the roof and the two sides, while the rock strength of siltstone in the roof is significantly greater than that in the two sides, so the damage of coal seams in the two sides is more serious than that in the two sides. Since no support measures are taken for the bottom plate, the plastic area of the bottom plate is not significantly reduced. From the plastic zone of the bottom plate, it can be seen that the failure mode of the outermost layer is roughly the same as the basic failure mode (Section 4.1).

Figure 8 presents the stress distribution diagram of the roadway before and after the original support. From Figures 8(a) and 8(b), we can see the change of the cloud diagram of the maximum principal stress distribution before and after the support. The biggest change is that the stress concentration area after the support shrinks to the roadway surface. Combined with these two diagrams, we can see that the stress concentration area of the roof shrinks most obviously to the roadway surface after the support, while the stress cloud diagram of the floor has little change, which is mainly due to the strong support of the roof. No support measures are taken for the bottom plate. The change of the maximum principal stress nephogram before and after support is mainly due to the obvious reduction of the plastic area of the roof and two sides, while the stress concentration area exists in the complete rock stratum close to the failure area. Therefore, the stress concentration area of the two sides and roof shrinks to the roadway surface, while the stress concentration area of the floor shrinks not significantly.

Figures 8(c) and 8(d) show the horizontal stress nephogram before and after support, respectively. From these two figures, it can be seen that after support, compared with before support, the shrinkage of the stress concentration area around the roadway is very obvious and close to the roadway surface.

Figures 8(e) and 8(f) are the cloud charts of vertical stress distribution before and after support, which are butterfly shaped. The biggest difference between before and after support is that the maximum vertical stress decreases significantly, and the stress concentration area shrinks to the roadway surface. The maximum principal stress is decreased by nearly 11% from 32.5 MPa before support to 28.9 MPa after support, but the shrinkage of the stress concentration area of the floor is not obvious. At the same time, there is a stress reduction area at the lower part of the floor, which is mainly due to the upward stress formed in the surrounding rock of the floor after roadway excavation. In mechanics, this is mainly the result of wedge balance.

Figures 8(g) and 8(h) show the shear stress distribution nephogram before and after support. It can be seen that there are stress concentration areas at the shoulder and bottom corners of the roadway before and after roadway support. These four stress concentration areas are symmetrically distributed. Similarly, the stress concentration area shrinks and moves closer to the roadway surface after support, and the shear stress distribution nephogram after support is fuller. The maximum shear stress after support is reduced from 8.6 MPa before support to 7.4 MPa, which is significantly reduced by nearly 14%. This greatly optimizes the stress characteristics of roadway surrounding rock and can well reduce the area of plastic zone of roadway surrounding rock. Similarly, the change of shear stress distribution nephogram at the bottom plate is lighter than that at the top plate.

From these Figure 8, it can be seen that the original support has greatly optimized the stress structure of the roadway compared with the nonsupport, so that the stress concentration area around the roadway is close to the roadway, and the stress concentration coefficient is also reduced. However, it has little impact on the stress condition of the surrounding rock at the roadway floor, which is mainly because the floor has not taken any support measures. Therefore, support measures must be taken to improve the stress characteristics of the surrounding rock of the whole roadway.

Figures 9(a) and 9(b) show the horizontal displacement before and after support. It can be seen that not only the

Downloaded from http://pubs.geoscienceworld.org/gsa/lithosphere/article-pdf/doi/10.2113/2022/3810988/5659685/3810988.pdf
by guest

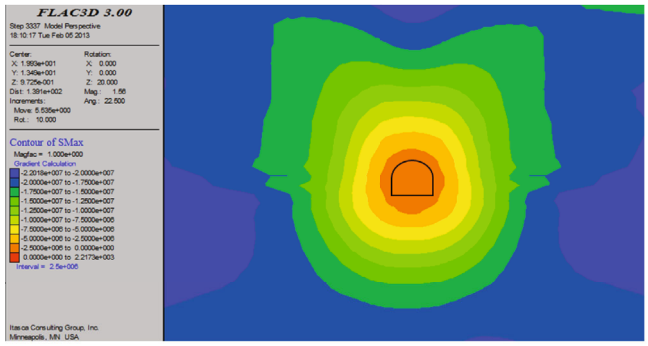

(a) Maximum principal stress diagram without support

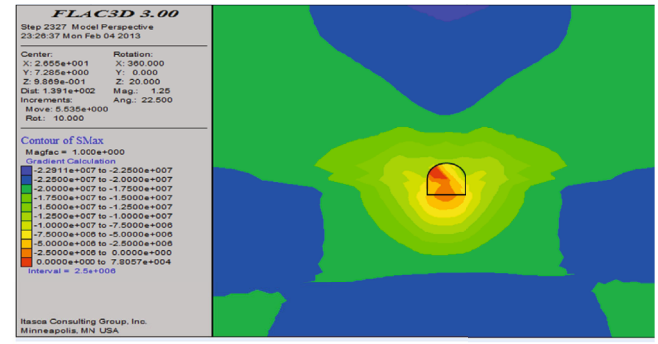

(b) Maximum principal stress diagram of originalsupport

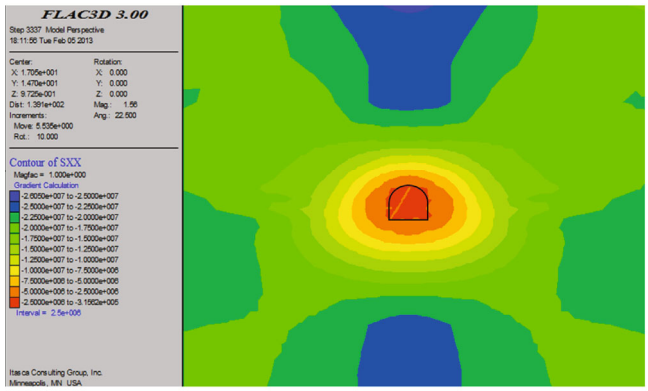

(c) Unsupported horizontal stress diagram

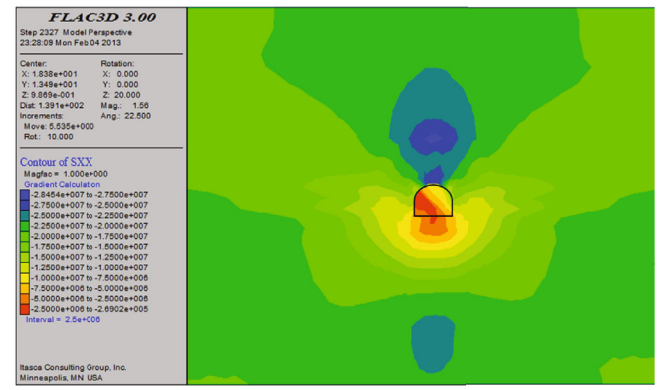

(d) Horizontal stress diagram of original support

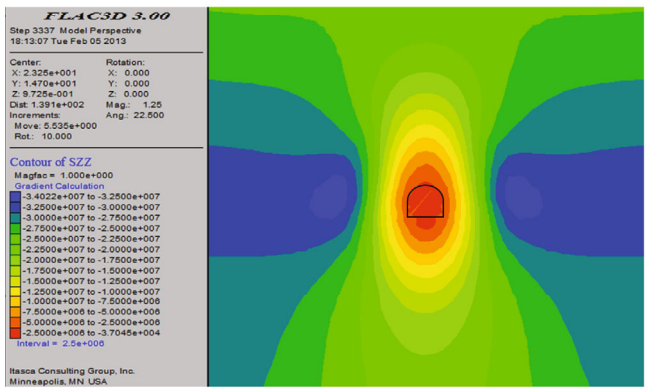

(e) Unsupported vertical stress diagram

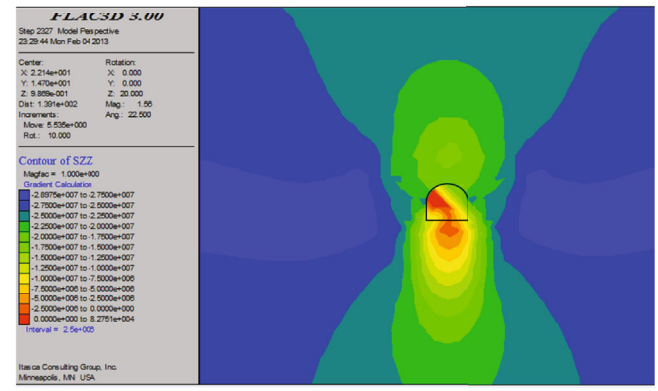

(f) Vertical stress diagram of original support

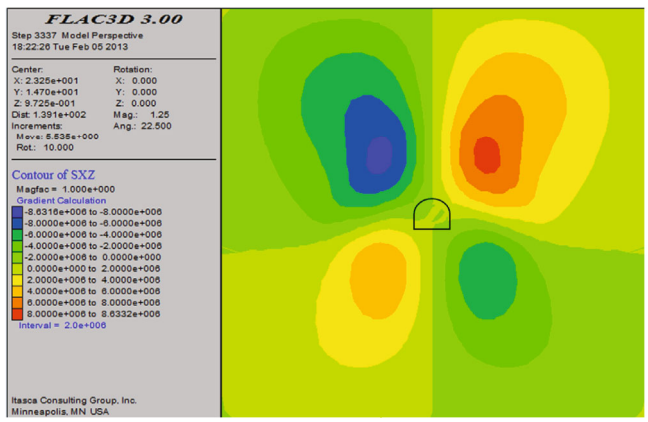

(g) Unsupported shear stress diagram

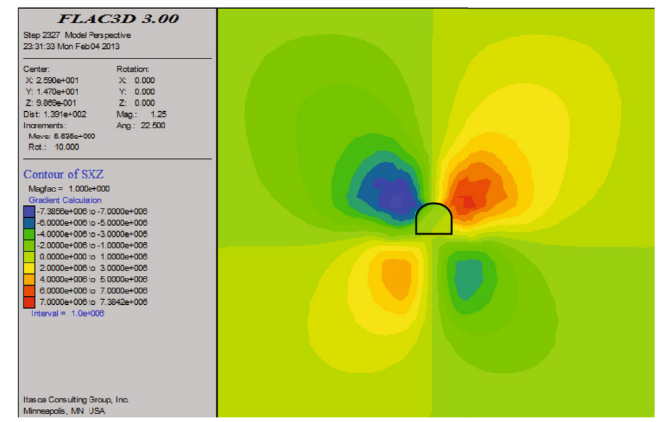

(h) Shear stress diagram of original support

Figure 8: Simulated stress distribution.

Downloaded from http://pubs.geoscienceworld.org/gsa/lithosphere/article-pdf/doi/10.2113/2022/3810988/5659685/3810988.pdf
by guest

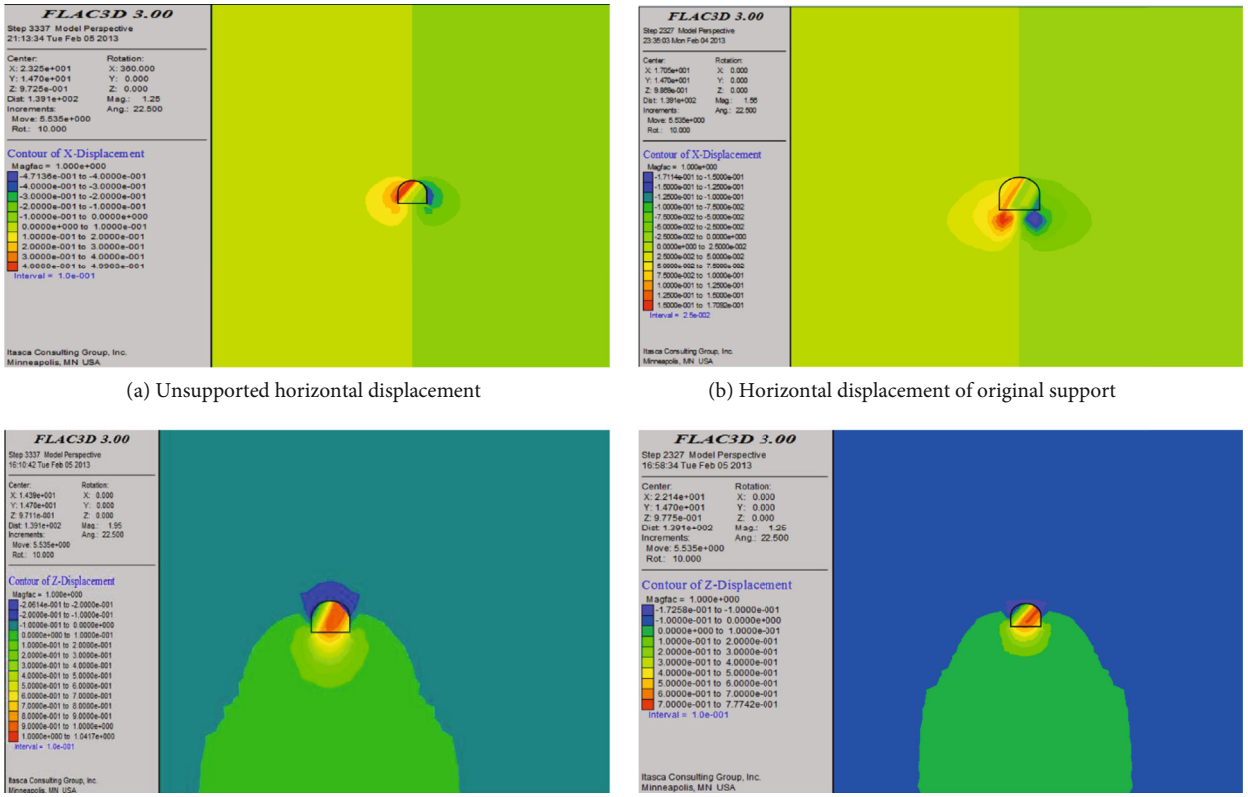

(a) Unsupported horizontal displacement

(b) Horizontal displacement of original support

(c) Unsupported vertical displacement

(d) Vertical displacement of original support

Figure 9: Simulated displacement diagram.

maximum horizontal displacement changes greatly before and after support but also the position of the maximum horizontal displacement changes. The maximum horizontal displacement is 471 mm before support and 171 mm after support. The displacement before and after support is reduced by 64%. The maximum horizontal displacement before support occurs at the position where the two sides of the roadway are close to the floor. The maximum horizontal displacement after support occurs at the bottom corner of the roadway floor. This is mainly because the bolt shotcrete support system limits the displacement of the two sides, but the floor does not take any support measures. The displacement of the two sides of the roadway is greater than the bottom corner of the roadway floor, but after the bolt shotcrete support is adopted, the displacement of the two sides is limited. The horizontal displacement at the bottom corner of the floor is not limited, resulting in the horizontal displacement at the bottom corner of the floor exceeding the horizontal displacement of the floor of the two sides of the roadway.

Figures 9(c) and 9(d) show the vertical displacement before and after support. After adopting the original support parameters, the maximum displacement of roadway roof is reduced from 201 mm to 170 mm, a decrease of 15%, and the floor displacement is limited, from 1000 mm to 770 mm, a decrease of 23%. From this, it can be seen that the original support system not only well limits the roof displacement but also the floor displacement. However, after the original support is adopted, the displacement of the floor is still large, which is still destructive floor heave, which cannot meet the use requirements of the roadway. The maximum floor heave measured in the field is 750 mm, which is close to the roadway floor heave obtained by simulation, indicating that the model can well reflect the field situation, which also lays a foundation for the optimization of support parameters later.

5.2.2. Analysis of Failure Factors of Original Support. According to the above analysis and the data collected on site, we can see that the bottom heave of the third section of the winch lane in the third mining area of Qitaihe Longhu coal mine is mainly determined by the following aspects:

(1) Geological conditions

It can be seen from Table 3 that the mechanical strength of the floor surrounding rock of this roadway is low. It can be seen from the rock strata exposed during the excavation of this roadway that the bedding of several rock strata near the roadway is relatively developed, there are many sliding surfaces, the rock mass is easy to be broken, and the overall strength of the rock mass is low. Moreover, the occurrence depth of the surrounding rock of this roadway is large, and it is located in the protective coal pillar up the mountain. In the stress concentration area of this mining area, the surrounding rock of the roadway is greatly affected by mining.

Downloaded from http://pubs.geoscienceworld.org/gsa/lithosphere/article-pdf/doi/10.2113/2022/3810988/5659685/3810988.pdf
by guest

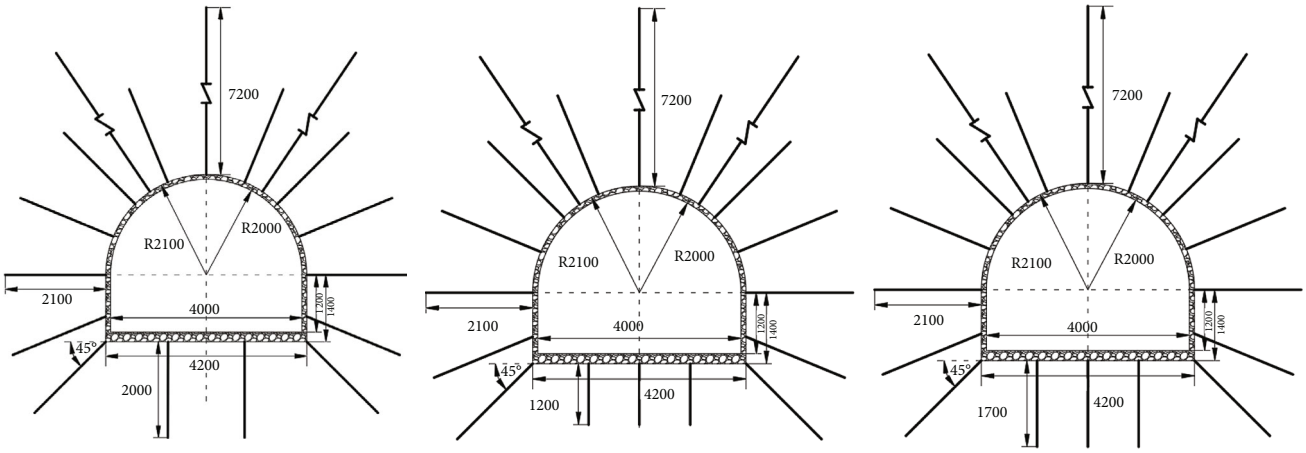

(a) Scheme 1 (b) Scheme 2 (c) Scheme 3

Figure 10: Support scheme diagram.

(2) Support design

In deep mining, the roadway in high stress environment is different from that in shallow mining, so secondary or even more coupling support must be used. The third section of the winch lane in the third mining area of rulonghu mine adopts the form of bolt shotcrete net + anchor cable support. However, due to the decoupling between the support and the surrounding rock, the roadway has large deformation such as roof subsidence, roof fall, and spray layer falling off. In the deep high stress mechanical environment, without any support measures, the roadway floor will become the main channel for energy release, resulting in the extrusion of rock blocks at the bottom corner of the roadway to the adjacent space of the roadway, causing the subsidence of both sides of the roadway, which further aggravates the deformation of the roadway roof and further worsens the properties of surrounding rock.

Inadequate construction quality

(3) Bolt shotcrete mesh support

It is difficult to directly judge the support quality in appearance, so it is difficult to evaluate the support quality. In construction, if the anchor bolt is not installed in place, the anchoring force and preload cannot meet the requirements, and the networking quality cannot pass, it will directly affect the support effect.

5.2.3. Roadway Support Optimization. Compared with no support, the original support system has played a great role in reducing the area of plastic zone, increasing the integrity of surrounding rock, optimizing the stress state around the roadway, reducing the stress concentration factor, and reducing the deformation of the roadway. Especially, after adopting the original support parameters, it has played a great role in the development of plastic zone of roof and two sides, the nearby stress concentration factor, and the limitation of horizontal and vertical displacement; however, the floor heave is still destructive, so the support parameters of the original roadway must be optimized.

(1) Optimize the Support Scheme. According to the field experience, it is only necessary to limit the roadway floor heave within 200 mm to meet the normal production needs. On the basis of this floor heave, the length of the floor bolt shall be reduced as much as possible, so as to maximize the economic and technical benefits. Therefore, first, the variation of floor heave under different length of bolt support is simulated by FLAC3D numerical simulation software, so as to determine the optimal length of bolt for floor support. Figure 10 shows different support schemes.

Scheme 1: the bottom plate anchor bolt adopts a pair of bottom angle anchor bolts in each row plus two vertical anchor bolts. The angle of anchor rod at the bottom angle is 45° to the horizontal direction, the length of anchor rod is 2.0 m, the spacing between anchor rods is 1600 mm, and the spacing between rows is 1600 mm.

Scheme 2: the bottom plate anchor bolt adopts a pair of bottom angle anchor bolts in each row plus three vertical anchor bolts. The angle of bottom angle anchor bolts is 45° to the horizontal direction. The anchor bolt length is 1.2 m, the anchor bolt spacing is 1000 mm, and the row spacing is 1000 mm.

Scheme 3: the base plate anchor bolt adopts a pair of bottom angle anchor bolts in each row plus three vertical anchor bolts. The angle of bottom angle anchor bolts is 45° to the horizontal direction. The anchor bolt length is 1.7 m, the anchor bolt spacing is 1000 mm, and the row spacing is 1000 mm.

(2) Support Effect of Optimized Scheme. Figures 11 (a)–11(c) show the range of plastic zone of surrounding rock under different support. From these three figures, we can see that when the bottom plate is supported by bolts, not only the area of plastic zone of bottom plate is greatly reduced but also the area of plastic zone of two sides is significantly

Downloaded from http://pubs.geoscienceworld.org/gsa/lithosphere/article-pdf/doi/10.2113/2022/3810988/5659685/3810988.pdf
by guest

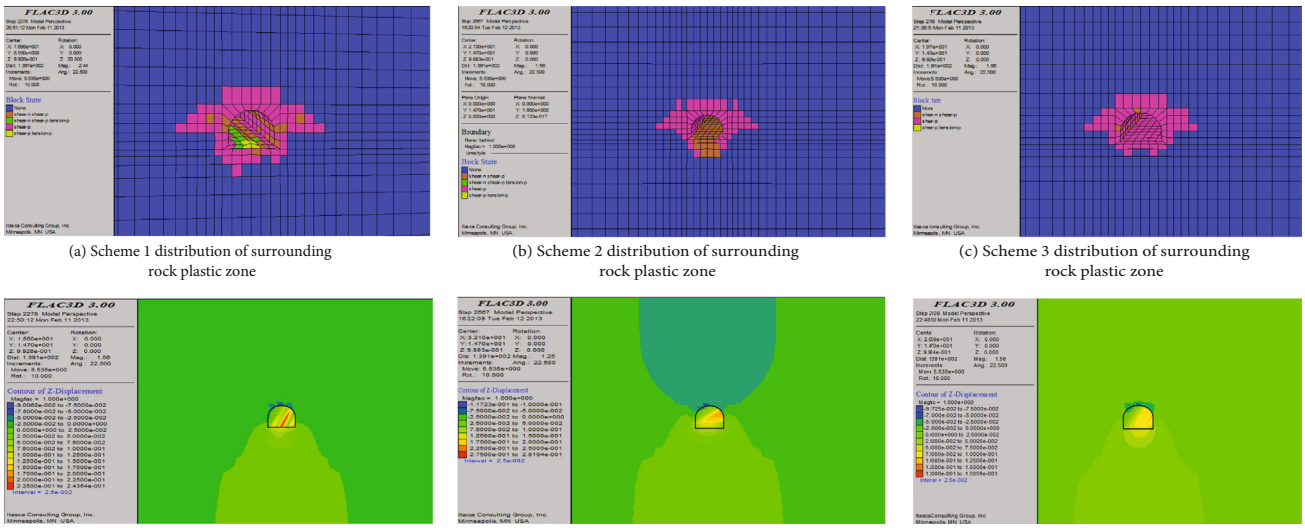

(a) Scheme 1 distribution of surrounding rock plastic zone

(b) Scheme 2 distribution of surrounding rock plastic zone

(c) Scheme 3 distribution of surrounding rock plastic zone

(d) Scheme1 vertical displacement diagram

(e) Scheme 2 vertical displacement diagram

(f) Scheme 3 vertical displacement diagram

Figure 11: Supporting effect drawing of each scheme.

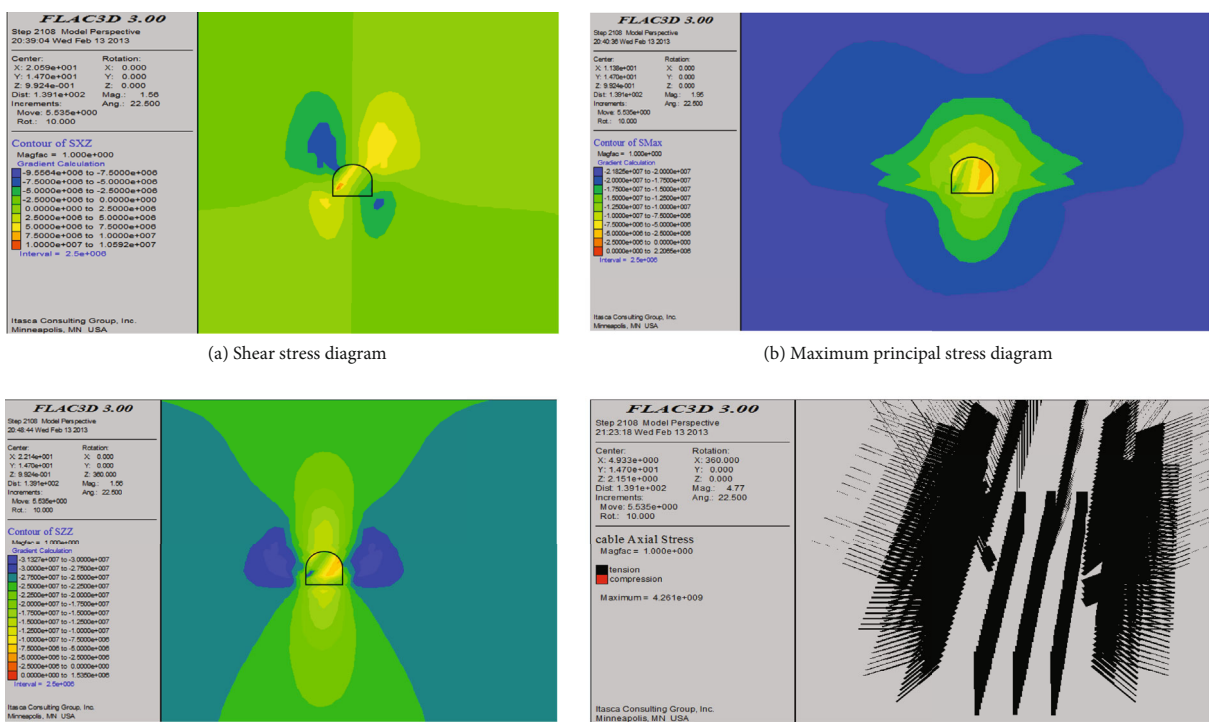

(a) Shear stress diagram

(b) Maximum principal stress diagram

(c) Vertical stress diagram

(d) Bolt stress diagram

Figure 12: Scheme 3 support effect drawing.

reduced. At the same time, the floor heave of the roadway has been obviously controlled. Therefore, in the area where the floor heave of the roadway is more serious, if the bolt support is adopted in the floor of the roadway like the two sides and the roof, the floor heave of the roadway can be limited to a great extent. It can be seen from Figure 11 that the plastic zone range of scheme 3 is similar to that of scheme 1, and the plastic zone range of scheme 2 is the largest. In terms of failure mode, the bottom plates of scheme 2 and scheme 3 are damaged by shear, while the bottom plates of scheme 1 are also damaged by tension. Therefore, the bottom plates of scheme 2 and scheme 3 are relatively flat, while the bottom plates of scheme 1 can see obvious irregular uplift. The floor slab and the amount of deformation of the track do not meet the requirements of scheme I, but the floor slab does not meet the requirements of scheme 1.

Figures 11(d)–11(f) show the cloud diagram of the vertical displacement distribution of the surrounding rock of the roadway under each support scheme. When the roadway

Downloaded from http://pubs.geoscienceworld.org/gsa/lithosphere/article-pdf/doi/10.2113/2022/3810988/5659685/3810988.pdf
by guest

floor is supported by bolts, the roadway floor heave is greatly reduced. The maximum floor heave of the original support is 770 mm, and the maximum floor heave of scheme 2 is 281 mm, which is reduced by 63%, and the maximum floor heave of scheme 3 is 150 mm, which is reduced by 81%. The roadway floor displacement of scheme 2 and scheme 3 is relatively balanced, which is consistent with the roadway floor leveling in Figures 11(a)–11(c). After the support of the bottom plate, it can also well limit the displacement of the top plate. Before supporting the floor, the maximum displacement of the roadway roof is 172 mm, while the maximum displacement of the roof in scheme 1, 2, and 3 is 90 mm, 117 mm, and 92 mm, respectively, reducing 52%, 68%, and 53%, respectively.

Through the displacement nephogram of the roadway surrounding rock floor without support and after bolt support, it can be clearly seen that the bolt support of the floor is very obvious to limit the floor heave. After support, the stress condition of roadway has been significantly improved, and the stress range of roadway surrounding rock has been significantly reduced. Compared with the original roadway support area, the surrounding rock of the roadway tends to be plastic and stable. Through the comparison between schemes, the optimal support parameters of roadway surrounding rock are obtained. Finally, the support mode of roadway floor is determined as the support mode of scheme 3.

(3) Stress Analysis of Surrounding Rock under Scheme 3 Support. Figure 12 shows the support effect of roadway surrounding rock under the support of scheme 3. Comparing these figures with the stress diagram under the original support scheme, we can clearly see the change of roadway surrounding rock stress under the support of scheme 3 and the original support system. First, the shrinkage of the stress concentration area of the roadway floor is the most obvious. The concentration areas are close to the roadway surface in varying degrees, and the maximum stress also decreases in varying degrees. Due to the support of the floor, the stress nephogram of the roof and floor is symmetrical up and down, which is very close to the stress state around the hole in elasticity. Therefore, under the support of scheme 3, the stress state of roadway surrounding rock is more reasonable than that of roadway surrounding rock under the original support system.

6. Conclusion

In this paper, aiming at the floor heave problem of the three section winch lane in the third mining area of Longhu coal mine in Qitaihe, first, the field investigation is carried out, the rock samples in the floor heave area are collected, and the mechanical properties are tested, which provide the calibration of mechanical parameters for the establishment of the model, and the floor heave problem of the roadway is studied. The main conclusions are as follows:

(1) Aiming at the problem of floor stability, this paper establishes a stability analysis method of roadway floor by analogy with the base heave of deep foundation pit from the flow rule under Mohr-Coulomb yield criterion and the sliding surface of Prandall-Riesner solution, analyzes the mechanism of floor heave in theory, and puts forward a safety factor K for roadway floor heave

(2) Through the rock parameters measured in the field and laboratory, FLAC3D numerical simulation software is used to simulate the stress and strain states of the semicoal rock roadway under various support modes and in various ranges of surrounding rock loose circle. The simulation results show that the floor heave of the roadway under the original support is reduced by 23%, but the maximum floor heave is still 770 mm, which is similar to the measured floor heave of 750 mm. This finding indicates that the simulation can better reflect the field situation

(3) Considering the economy, this paper provides three kinds of roadway support methods. By simulating the stress and strain states of roadway and the range of surrounding rock loose circle with various roadway support measures, the optimal scheme is finally determined. Compared with the floor heave in original optimal support scheme, the floor heave of roadway is reduced by 81%, and the final floor heave is 150 mm, which can meet the deformation requirements of roadway floor. The results provide a guidance for the support optimization of semicoal rock roadway

Data Availability

The datasets used and/or analyzed during the current study are available from the corresponding author on reasonable request.

Conflicts of Interest

The authors declare no competing interests.

Authors' Contributions

Xuming Zhou, Sheng Wang, and Xuelong Li proposed the research. Jing Meng and Zhen Li prepared figures and tables and interpreted the structural data. Linhan Zhang, Dongdong Pu, and Longkang Wang developed the main ideas. All coauthors actively contributed to the manuscript with comments, ideas, and suggestions. All authors have read and agreed to the published version of the manuscript.

Acknowledgments

This study was financially supported by the National Natural Science Foundation of China (52104204) and Natural Science Foundation of Shandong Province (ZR2021QE170).

Downloaded from http://pubs.geoscienceworld.org/gsa/lithosphere/article-pdf/doi/10.2113/2022/3810988/5659685/3810988.pdf
by guest

References

[1] X. Yu, Y. Liu, and H. Fan, "Influence of coal seam floor damage on floor damage depth," *Environmental Earth Sciences*, vol. 81, no. 6, p. 182, 2022.

[2] S. Mo, P. Sheffield, P. Corbett et al., "A numerical investigation into floor buckling mechanisms in underground coal mine roadways," *Tunnelling and Underground Space Technology*, vol. 103, no. 5, article 103497, 2020.

[3] S. F. Wang, Y. Tang, X. B. Li, and D. U. Kun, "Analyses and predictions of rock cuttabilities under different confining stresses and rock properties based on rock indentation tests by conical pick," *Transactions of the Nonferrous Metals Society of China*, vol. 31, no. 6, pp. 1766–1783, 2021.

[4] L. M. Qiu, Z. T. Liu, E. Y. Wang, X. He, J. Feng, and B. Li, "Early-warning of rock burst in coal mine by low-frequency electromagnetic radiation," *Engineering Geology*, vol. 279, no. 5, article 105755, 2020.

[5] X. L. Li, S. J. Chen, S. Wang, M. Zhao, and H. Liu, "Study on in situ stress distribution law of the deep mine: taking Linyi mining area as an example," *Advances in Materials Science and Engineering*, vol. 2021, Article ID 5594181, 11 pages, 2021.

[6] A. Kumar, P. Waclawik, R. Singh, S. Ram, and J. Korbel, "Performance of a coal pillar at deeper cover: field and simulation studies," *International Journal of Rock Mechanics and Mining Sciences*, vol. 113, pp. 322–332, 2019.

[7] S. Q. Yang, M. Chen, H. W. Jing, K. F. Chen, and B. Meng, "A case study on large deformation failure mechanism of deep soft rock roadway in Xin'An coal mine, China," *China. Engineering Geology*, vol. 217, pp. 89–101, 2017.

[8] J. Chang, D. Li, T. Xie, W. Shi, and K. He, "Deformation and failure characteristics and control technology of roadway surrounding rock in deep coal mines," *Geofluids*, vol. 2020, Article ID 8834347, 15 pages, 2020.

[9] F. Gao, D. Stead, H. Kang, and Y. Wu, "Discrete element modelling of deformation and damage of a roadway driven along an unstable goaf – a case study," *International Journal of Coal Geology*, vol. 127, pp. 100–110, 2014.

[10] G. Guo, H. Kang, D. Qian, F. Gao, and Y. Wang, "Mechanism for controlling floor heave of mining roadways using reinforcing roof and sidewalls in underground coal mine," *Sustainability*, vol. 10, no. 5, p. 1413, 2018.

[11] X. Kang, D. Guo, and Z. Lu, "Mechanism of roadway floor heave controlled by floor corner pile in deep roadway under high horizontal stress," *Advances in Civil Engineering*, vol. 2021, Article ID 6669233, 10 pages, 2021.

[12] S. Mo, H. L. Ramandi, J. Oh et al., "A new coal mine floor rating system and its application to assess the potential of floor heave," *International Journal of Rock Mechanics and Mining Sciences*, vol. 128, article 104241, 2020.

[13] X. M. Sun, F. Chen, M. C. He, W. L. Gong, H. C. Xu, and H. Lu, "Physical modeling of floor heave for the deep-buried roadway excavated in ten degree inclined strata using infrared thermal imaging technology," *Tunnelling and Underground Space Technology*, vol. 63, pp. 228–243, 2017.

[14] Q.-S. Liu, X. W. Liu, X. Huang, and B. Liu, "Research on the floor heave reasons and supporting measures of deep soft-fractured rock roadway," *Journal of China Coal Society*, vol. 38, no. 4, pp. 566–571, 2013.

[15] J. B. Bai and C. J. Hou, "Control principle of surrounding rocks in deep roadway and its application," *Journal of China University of Mining & Technology*, vol. 35, no. 2, pp. 145–148, 2006.

[16] J. B. Bai, X. F. Li, X. Y. Wang, Y. Xu, and L. J. Huo, "Mechanism of floor heave and control technology of roadway induced by mining," *Journal of Mining & Safety Engineering*, vol. 28, no. 1, pp. 1–5, 2011.

[17] X. H. Li, Z. B. Huang, and H. M. Yang, "Stress transfer technique of controlling chamber's floor heave under high mining stress," *Journal of China University of Mining & Technology*, vol. 35, no. 3, pp. 296–300, 2006.

[18] X. H. Li, W. J. Wang, and C. J. Hou, "Controlling floor heave with strengthening roof in gateway by numerical analysis," *Journal of China University of Mining & Technology*, vol. 32, no. 4, pp. 98–101, 2003.

[19] C. Zhao, Y. Li, G. Liu, and X. Meng, "Mechanism analysis and control technology of surrounding rock failure in deep soft rock roadway," *Engineering Failure Analysis*, vol. 115, no. 9, article 104611, 2020.

[20] C. J. Hou, "Key technologies for surrounding rock control in deep roadway," *Journal of China University of Mining & Technology*, vol. 46, no. 5, pp. 970–978, 2017.

[21] G. Wu, W. Chen, S. Jia et al., "Deformation characteristics of a roadway in steeply inclined formations and its improved support," *International Journal of Rock Mechanics and Mining Sciences*, vol. 130, no. 3-4, article 104324, 2020.

[22] J. Shi, C. A. You, C. Xuan, L. Yang, and D. B. Bi, "Effect of the inverted arch manner props in the mining roadway based on the maximum plastic limit analysis," *Journal of Safety and Environment*, vol. 16, no. 4, pp. 139–143, 2016.

[23] M. X. Chu, Q.-B. Wang, and J.-M. Xia, "Study of formation mechanism of floor heave at goaf side of roadway and prevention technology," *Rock and Soil Mechanics*, vol. 32, no. S2, pp. 413–417, 2011.

[24] L. Shi, H. Zhang, and P. Wang, "Research on key technologies of floor heave control in soft rock roadway," *Advances in Civil Engineering*, vol. 2020, Article ID 8857873, 13 pages, 2020.

[25] B. H. Guo and T. K. Lu, "Analysis of floor heave mechanism and cutting control technique in deep mines," *Journal of Mining & Safety Engineering*, vol. 1, pp. 91–94, 2008.

[26] X. Zhang, J. Hu, H. Xue et al., "Innovative approach based on roof cutting by energy-gathering blasting for protecting roadways in coal mines," *Tunnelling and Underground Space Technology*, vol. 99, no. 191, article 103387, 2020.

[27] Y. Kang, Q. Liu, G. Gong, and H. Wang, "Application of a combined support system to the weak floor reinforcement in deep underground coal mine," *International Journal of Rock Mechanics and Mining Sciences*, vol. 71, pp. 143–150, 2014.

[28] S. F. Wang, Y. Tang, and S. Y. Wang, "Influence of brittleness and confining stress on rock cuttability based on rock indentation tests," *Journal of Central South University*, vol. 28, no. 9, pp. 2786–2800, 2021.

[29] Y. Y. Jiao, L. Song, X. Z. Wang, and A. Coffi Adoko, "Improvement of the U-shaped steel sets for supporting the roadways in loose thick coal seam," *International Journal of Rock Mechanics and Mining Sciences*, vol. 60, pp. 19–25, 2013.

[30] S. Kędzior and I. Jelonek, "Reservoir parameters and maceral composition of coal in different carboniferous lithostratigraphical series of the Upper Silesian Coal Basin, Poland," *Poland. International Journal of Coal Geology*, vol. 111, pp. 98–105, 2013.

[31] Y. Yu, S. E. Chen, K. Z. Deng, and H. D. Fan, "Long-term stability evaluation and pillar design criterion for room-and-pillar mines," *Energies*, vol. 10, no. 10, p. 1644, 2017.

Downloaded from http://pubs.geoscienceworld.org/gsa/lithosphere/article-pdf/doi/10.2113/2022/3810988/5659685/3810988.pdf
by guest

[32] M. Bukowska, P. Kasza, R. Moska, and J. Jureczka, "The Young's modulus and Poisson's ratio of hard coals in laboratory tests," *Energies*, vol. 15, no. 7, p. 2477, 2022.

[33] L. Qiu, Y. Zhu, D. Song et al., "Study on the nonlinear characteristics of EMR and AE during coal splitting tests," *Minerals*, vol. 12, no. 2, p. 108, 2022.

[34] S. M. Liu, X. L. Li, D. K. Wang, and D. Zhang, "Investigations on the mechanism of the microstructural evolution of different coal ranks under liquid nitrogen cold soaking," *Energy Sources, Part A: Recovery, Utilization, and Environmental Effects*, pp. 1–17, 2020.

[35] X. L. Li, S. J. Chen, S. M. Liu, and Z. H. Li, "AE waveform characteristics of rock mass under uniaxial loading based on Hilbert-Huang transform," *Journal of Central South University*, vol. 28, no. 6, pp. 1843–1856, 2021.

[36] M. J. Jiang, W. Fang, and J. Sima, "Calibration of micro-parameters of parallel bonded model for rocks," *Journal of Shandong University (Engineering Science)*, vol. 41, no. 4, pp. 50–56, 2015.

[37] L. Li, M. J. Jiang, and F. G. Zhang, "Quantitative simulation of triaxial test considering residual strength on deep rock using DEM and parameter analysis," *Rock and Soil Mechanics*, vol. 39, no. 3, pp. 1082–1090+1099, 2018.

[38] Q. Ma, Y. Tan, X. Liu, Q. Gu, and X. Li, "Effect of coal thicknesses on energy evolution characteristics of roof rock- coal-floor rock sandwich composite structure and its damage constitutive model," *Composites Part B: Engineering*, vol. 198, no. 1, article 108086, 2020.

[39] X. H. Li, Y. Long, C. Ji, X. Zhou, Y. Y. He, and L. Lu, "Analysis of dynamic stress concentration factor for existing circular tunnel lining under blasting seismic wave," *Rock and Soil Mechanics*, vol. 34, no. 8, pp. 2218–2224, 2013.

[40] H. Li, B. Lin, Y. Hong et al., "Effects of in-situ stress on the stability of a roadway excavated through a coal seam," *International Journal of Mining Science and Technology*, vol. 27, no. 6, pp. 917–927, 2017.

[41] X. Lai, H. Xu, P. Shan, Y. Kang, Z. Wang, and X. Wu, "Research on mechanism and control of floor heave of mining-influenced roadway in top coal caving working face," *Energies*, vol. 13, no. 2, p. 381, 2020.

[42] S. Aghababaei, G. Saeedi, and H. Jalalifar, "Risk analysis and prediction of floor failure mechanisms at longwall face in parvadeh-i coal mine using rock engineering system (RES)," *Rock Mechanics and Rock Engineering*, vol. 49, no. 5, pp. 1889–1901, 2016.

[43] Y. D. Jiang, Y. X. Zhao, and W. G. Liu, "Research on floor heave of roadway in deep Mingin," *Chinese Journal of Rock Mechanics and Engineering*, vol. 23, no. 14, pp. 2396–2401, 2004.

[44] Y. J. Yin, X. L. Liu, and Y. M. Qian, "Research on the deformation monitoring of deep foundation pit engineering," *Advanced Materials Research*, vol. 889-890, no. 2, pp. 1383–1387, 2014.

[45] S. J. Yang, S. Zeng, and B. Sun, "Fuzzy reliability analysis of resistant heave stability for deep foundation pit based on deformation," *Chinese Journal of Underground Space and Engineering*, vol. 5, no. 3, p. 4, 2009.

[46] X. R. Meng, C. H. Xu, Z. N. Gao, and X. Q. Wang, "Stress distribution and damage mechanism of mining floor," *Journal of China Coal Society*, vol. 35, no. 11, pp. 1832–1836, 2010.

[47] Y. Jiang, D. Zhang, K. Wang, and X. Zhang, "Mining-induced damage characteristics of floors during fully mechanized caving mining: a case study," *Advances in Materials Science and Engineering*, vol. 2018, 11 pages, 2018.

[48] H. Y. Liu, B. Y. Zhang, X. L. Li et al., "Research on roof damage mechanism and control technology of gob-side entry retaining under close distance gob," *Engineering Failure Analysis*, vol. 138, no. 5, article 106331, 2022.

[49] S. B. Tang and C. A. Tang, "Numerical studies on tunnel floor heave in swelling ground under humid conditions," *International Journal of Rock Mechanics and Mining Sciences*, vol. 55, pp. 139–150, 2012.

[50] H. Hasanzadehshooiili, A. Lakirouhani, and J. Medzvieckas, "Evaluating elastic-plastic behaviour of rock materials using hoek–brown failure criterion," *Journal of Civil Engineering and Management*, vol. 18, no. 3, pp. 402–407, 2012.

[51] X. L. Li, S. J. Chen, Q. M. Zhang, X. Gao, and F. Feng, "Research on theory, simulation and measurement of stress behavior under regenerated roof condition," *Geomechanics and Engineering*, vol. 26, no. 1, pp. 49–61, 2021.

[52] K. H. Park and Y. J. Kim, "Analytical solution for a circular opening in an elastic-brittle-plastic rock," *International Journal of Rock Mechanics and Mining Sciences*, vol. 43, no. 4, pp. 616–622, 2006.

Downloaded from http://pubs.geoscienceworld.org/gsa/lithosphere/article-pdf/doi/10.2113/2022/3810988/5659685/3810988.pdf
by guest